Supporting Information for

Carbon quantum dots-embedded reduced graphene oxide compact films for highly pressure-tolerant electrodes

Dou Lin,[ab] Ziyan Zhou,[ab] Ronghao Shi,*[c] Bin Chen,[ab] Zhulin Huang,[ab] Haibin Tang,*[ab] Jun Wang,[d] Xiaoguang Zhu,[a] Cheng Shao[a] and Fangming Han*[ab]

[a] *Key Laboratory of Materials Physics, and Anhui Key Laboratory of Nanomaterials and Nanostructures, Institute of Solid State Physics, HFIPS, Chinese Academy of Sciences, Hefei, 230031, P. R. China.*
[b] *University of Science and Technology of China, Hefei, 230026, P. R. China.*
[c] *Henan Key Laboratory of Advanced Conductor Materials, Institute of Materials, Henan Academy of Sciences, Zhengzhou 450046, P. R. China.*
[d] *State Key Laboratory of Nonlinear Mechanics, Institute of Mechanics, Chinese Academy of Sciences, Beijing 100190, P. R. China.*

*Corresponding author.
E-mail address: F. Han (fmhan@issp.ac.cn), H. Tang (hbtang@issp.ac.cn) and R. Shi (smartsrh@hnas.ac.cn).

Experimental Section

Materials

Chemicals and materials: Sulfuric acid (H_2SO_4, AR grade, 95.0%～98.0% of purity) was purchased from Sinopharm Chemical Reagent Co., LTD. Sodium hydroxide (NaOH, AR grade, 96.0% of purity), and potassium hydroxide (KOH, AR grade, 95.0% of purity) were obtained from Aladdin Chemical Reagent Co., LTD. A 100 μm-thick NKK-MPF30AC-100 Separator was purchased from Nagano Industries Co., Ltd., Japan. We employed 200 μm-thick platinum foils sourced from Zhongnuo New Materials (Beijing) Technology Co., LTD. Graphene oxide (GO)solutions (2 mg/mL) were acquired from Shanxi Institute of Coal Chemistry, Chinese Academy of Sciences. Mixed cellulose (MCE) membranes (0.22 μm pore size) were obtained from Marbridge Biofilm Technology (Nantong) Co., LTD. Dialysis membranes were purchased from Changde BKMAM Biotechnology Co., LTD.

Biomaterials: Peanut shells were directly procured from a local farmer's market in Hefei, China. Magnolia leaves were collected from the garden of the Hefei Academy of Physical Sciences, Chinese Academy of Sciences. Wheat straws were gathered from a local agricultural field in Hefei, China.

Material synthesis S1: Preparation of carbon quantum dots (CQDs)

Hydrothermal treatment: One gram of biologic precursor (Peanut shells, magnolia leaves or wheat straws) was first added to 50 mL of a 3 M NaOH solution. The mixture was then transferred to a 100 mL Teflon-lined stainless-steel autoclave and hydrothermally treated at 185°C for 5 hours.

Purification: The reaction product was centrifuged at 10000 rpm for 10 minutes to remove precipitates. The resulting supernatant was collected and dialyzed against deionized water for one week using a dialysis membrane (BKMAMLAB, MD77-1000D) to remove residual impurities.

Freeze-drying: The dialysis solution was then collected and freeze-dried using a vacuum freeze dryer (Shandong Trimaran Instrument Co., LTD, ST-10N-60A) to obtain the powder.

Preparation of CQDs solution: Finally, the biomaterial-derived CQDs powder was re-dispersed in deionized water to form a 1 mg/mL solution for further characterization and applications.

Material synthesis S2: Preparation of compact reduced graphene oxide (rGO) and rGO/CQDs films

Reduced Graphene Oxide: A diluted GO solution (~0.05 mg/ml) was first hydrothermally reduced in a Teflon-lined autoclave at 185~200°C for 3 hours. The resulting rGO colloidal

solution was then vacuum-filtered onto an MCE membrane (pore size 0.22 μm) to subsequently obtain rGO films after removal of the MCE membranes.

rGO/CQDs Hybrid Nanosheets: Stable aqueous colloids of rGO/CQDs hybrid nanosheets were prepared using a similar approach. A mixture of GO, CQDs, and deionized water (mass ratio CQDs:GO = 0.2, 0.4, 0.6 and 0.8; solution concentration ~0.05 mg/mL) was sealed in a Teflon-lined autoclave and heated at 185~200°C for 3 hours. The resulting rGO/CQDs colloidal solution was then vacuum-filtered onto an MCE membrane to fabricate CQDs-embedded rGO (rGO/CQDs) films. Finally, the rGO/CQDs films were attained after removing the MCE membrane.

Method S1: Material characterization

The morphologies of all the samples were characterized using a field emission scanning electron microscope (FE-SEM, HitachiSU8020) and a transmission electron microscope (TEM, JEOLJEM-2010) with a 200 keV accelerated electron beam. The chemical compositions were analyzed by X-ray photoelectron spectroscopy (XPS) using an X-ray photoelectron spectrometer (Thermo ESCALAB 250Xi) with a monochromatic Al Kα X-ray source (hν = 1486.6 eV, X-ray beam spot is 500 μm). N_2 adsorption-desorption isotherms were measured on an Ommishop 100CX, Coulter at 77 K, and the specific surface areas were calculated using the Brunauer-Emmett-Teller (BET) method. FTIR spectra were collected using a Thermo Nicolet nexus-470 FTIR instrument.

Method S2: Electrochemical tests

The electrochemical properties were evaluated in a two-electrode system using either 1 M H_2SO_4 or 6 M KOH solutions as electrolyte. The assembly process involved the following steps:

Electrode preparation: A NKKMPF30AC-100 separator was sandwiched between two circular films (diameter: 1 cm) acting as electrodes. These electrodes were fabricated using platinum (Pt) foils as current collectors.

Cell assembly and encapsulation: The assembled structure (electrode/separator/electrode) was then immersed in the chosen electrolyte and placed within a polyester pouch. Finally, the sandwich-like supercapacitors were formed by heat-sealing the polyester package.

The cyclic voltammetry (CV), galvanostatic charge/discharge (GCD), and electrochemical impedance spectroscopy (EIS) were measured on electrochemical workstations (Zahner, Zennium or Shanghai Chenhua, CHI760E).

The areal (F/cm^2) and volumetric (F/cm^3) specific capacitance, as well as the volumetric energy (mWh/cm^2) and power (mW/cm^3) densities, and areal energy (mWh/cm^2) and power (mW/cm^3) densities were calculated from the GCD curves using

$$C_s = \frac{2 \cdot I \cdot \Delta t}{M \cdot \Delta V}, \quad (1)$$

$$E_s = \frac{1}{2 \times 3.6} \cdot \frac{I \cdot \Delta t}{M_{all} \cdot \Delta V} \cdot V^2, \quad (2)$$

and

$$P_s = 3600 \cdot \frac{E_s}{\Delta t}, \quad (3)$$

where I (A) is the discharge current, Δt (s) is the discharge time dependent on the ΔV (V), Δt (s) is the discharge time, M is the area (cm^2) or volume (cm^3) of single electrode, M_{all} is the area (cm^2) or volume (cm^3) of all electrodes in a two-electrode system, ΔV is the potential window excluding the voltage drop (IR), and V (V) is the potential window, respectively.

The normalized real (C') and imaginary (C'') capacitances depending on frequency were calculated from the EIS by

$$C' = \frac{-Im(Z)}{M \cdot \pi \cdot f \cdot |Z|^2} \quad (4)$$

and

$$C'' = \frac{Re(Z)}{M \cdot \pi \cdot f \cdot |Z|^2}, \quad (5)$$

where $Z = \sqrt{Re(Z)^2 + Im(Z)^2}$ is the complex impedance, f is the frequency, Re(Z) is the real part of the complex impedance, and Im(Z) is the imaginary part of the complex impedance, respectively.

The relaxation time constant τ_0, which represents the minimum time needed to discharge over 50% of the energy from the supercapacitor,[1, 2] is used to evaluate the charge/discharge capability, and calculated by

$$\tau_0 = 1/f_0, \quad (6)$$

where f_0 is the frequency at which the normalized C'' reaches its maximum.

Method S3: Calculation of pressures applied facility on the rGO/CQDs hybrid-films based supercapacitors

The pressure (P, MPa) applied facility on rGO/CQDs hybrid films tested in a two-electrode system is calculated by

$$P = \frac{T * g * 1000}{\pi D^2/4} * 10^{-6}, \quad (7)$$

Where $T = 0.72 * P_0$ is the oil cylinder pressure (Ton) of manual powder tablet press (YP-24S, JOSVOK (Tianjin, China) Technology Development Co., Ltd), 0.72 is the correction factor of manual powder tablet press, P_0 is the displayed manual powder tablet press (MPa), g (m/s^2) is the acceleration of gravity, and D is the diameter (m) of tested sample. All samples are cut into 1 cm of diameter circular pieces. The calculated pressures are displayed in Table S1.

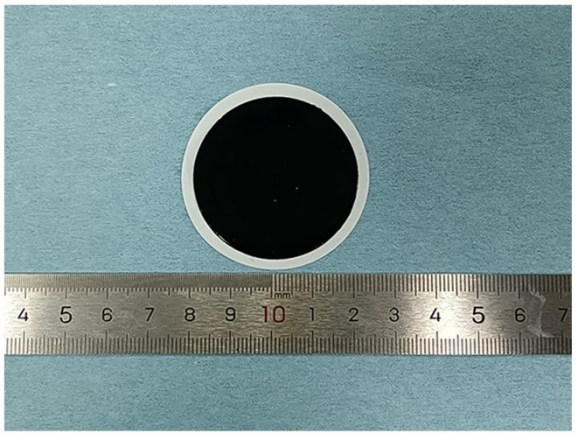

Fig. S1. Photograph of a compact rGO/CQDs hybrid film.

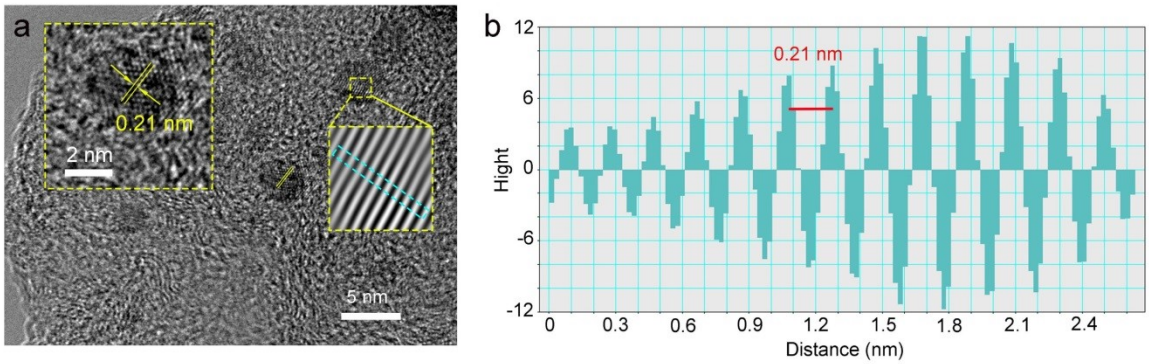

Fig. S2. (a) HRTEM image of rGO/CQDs hybrid nanosheet. (b) Lattice spacing of CQDs along the direction perpendicular to the lattice fringe (surrounded by a cyan rectangle box) in inset of (a).

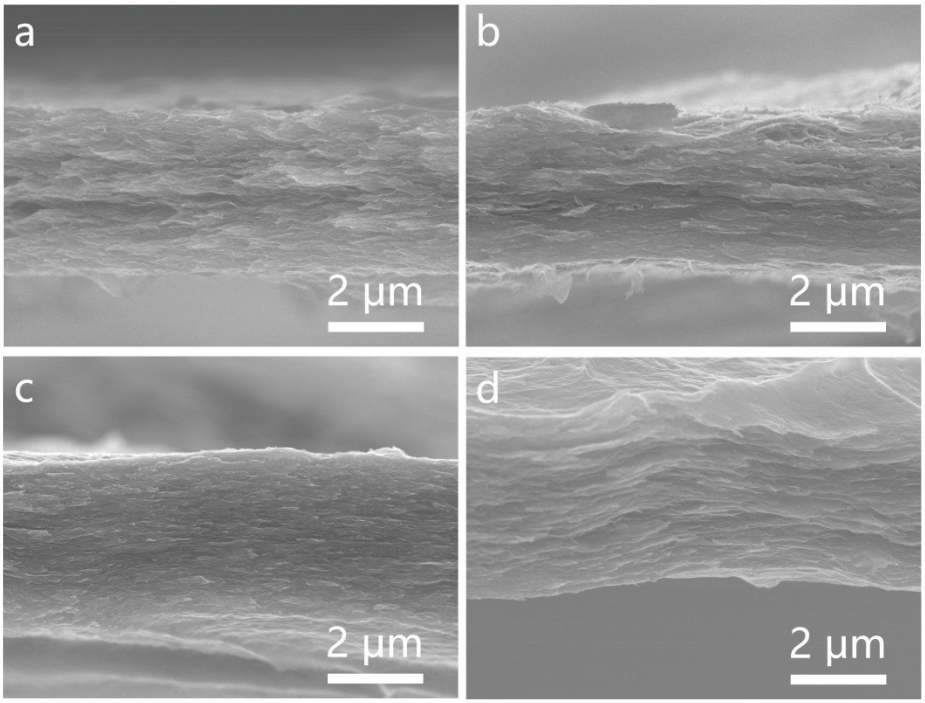

Fig. S3. Cross-sectional SEM images of rGO and compact rGO/CQDs hybrid films with different CQDs contents. (a) rGO, (b) rGO/CQDs-0.2, (c) rGO/CQDs-0.6 and d) rGO/CQDs-0.8. (the samples are signed as "rGO/CQDs-*X*", with *X* representing the mass ratio of CQDs/GO of crude materials used to make these electrodes)

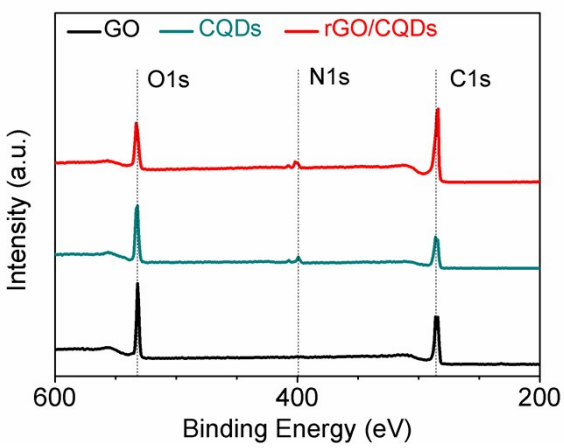

Fig. S4. XPS survey spectra of the GO, CQDs and rGO/CQDs (crude material mass ratio of CQDs/GO is 0.4).

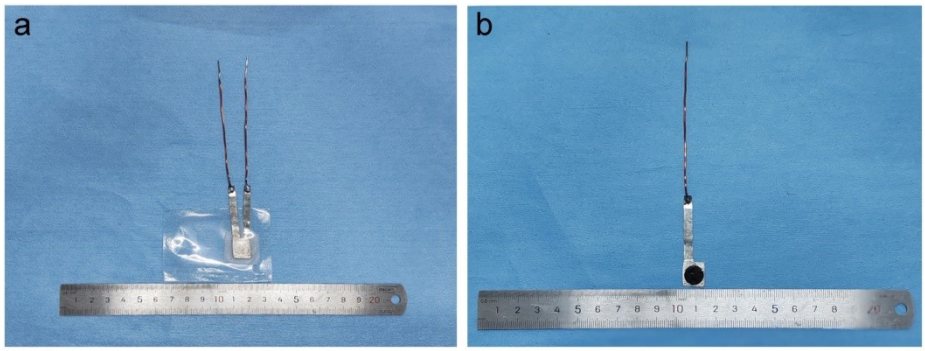

Fig. S5. Photograph of a sandwich-configuration supercapacitor (a) and a circular electrode on platinum foil (b).

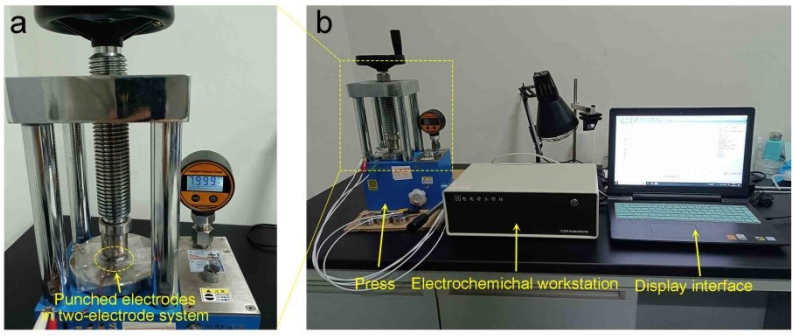

Fig. S6. Photograph of a synchronous electrochemical test of the sandwich-configuration supercapacitor under static pressures.

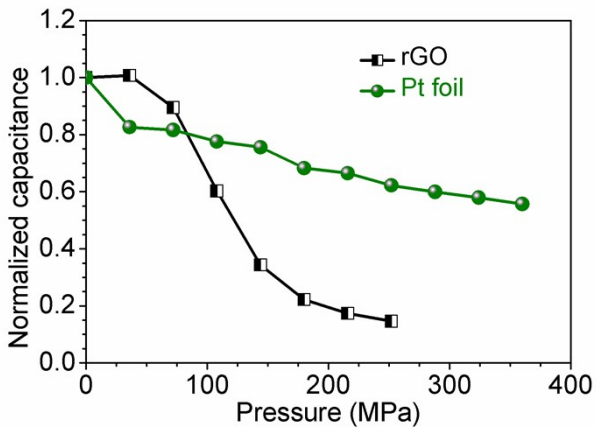

Fig. S7. Normalized capacitances of rGO and platinum foil as a function of increasing static pressure.

Prior to conducting the pressure-tolerant test, the potential buffering effect of the separator against compressive stress in a sandwich-configured supercapacitor was investigated. To assess the separator's influence on electrochemical properties, two smooth platinum (Pt) foils, each 100 μm-thick, were assembled into a sandwich-like supercapacitor using the same separator. This assembly was then tested under pressures ranging from 0 to 360 MPa.

The Nyquist plots for the Pt foil reveal an increase in series resistance (R_s) with increasing pressure (Fig. S8). R_s, presented by the point where the real axis intersects the Nyquist curve at high frequencies, rises from 0.6 to 2.0 ohms. The R_s is related to the electrolyte's ionic conductivity, the ohmic resistance of the electrodes and current collectors, and the contact resistance at the electrode material/current collector interface.[3] Since the electronic conductivity of the Pt foil remains constant, and no R_{ct} is observed in the Nyquist plots across the entire pressure range from 0 to 360 MPa. The slightly increased R_s can be solely attributed to the decreasing ion conductivity of the electrolyte in separator. This suggests that a slowly collapse of the separator's macroporous structure under pressure. In contrast, for the rGO-based supercapacitor, both R_s and R_{ct} exhibit significant increase with rising pressure (0 to 252 MPa). With the increase of R_s from 0.8 to 6.9 ohm, R_{ct} dramatically grows from 1.0 to 19.2 ohms (Fig. S17). This indicates a severe blockage of the ion transport pathways within the rGO electrode under a higher pressure, likely due to damage of its porous structure. Consequently, the capacitance of the rGO electrode decreases much faster than that of the Pt foil as pressure increases (Fig. S8). This behavior demonstrates that the separator can’t prevent or mitigate the high-pressure-induced damage to the electrode’s porous structure. These findings conclusively show that the separator offers no significant buffering effect against compressive pressure.

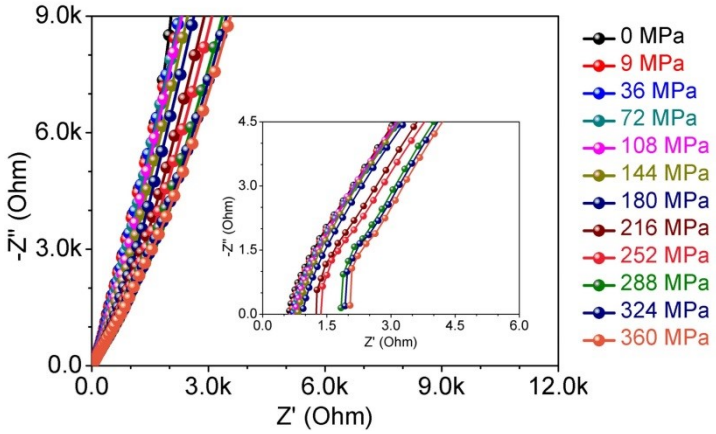

Fig. S8. Nyquist plots for the platinum foil-based supercapacitor at static pressures ranging from 0 to 360 MPa.

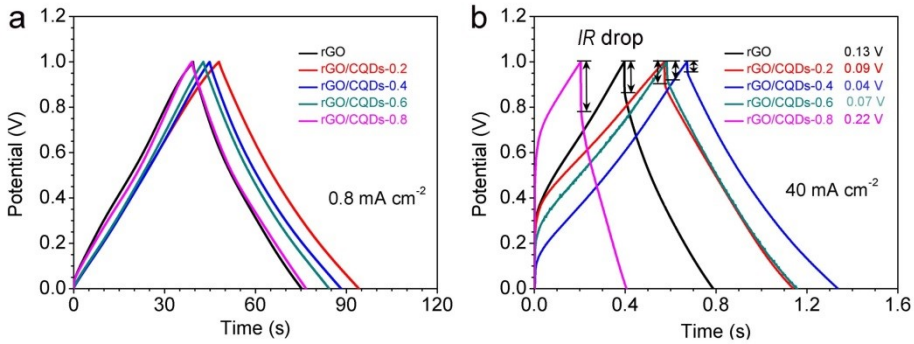

Fig. S9. Galvanostatic charge-discharge curves at 0.8 mA/cm^2 (a) and 40 mA/cm^2 (b), respectively (No pressure applied).

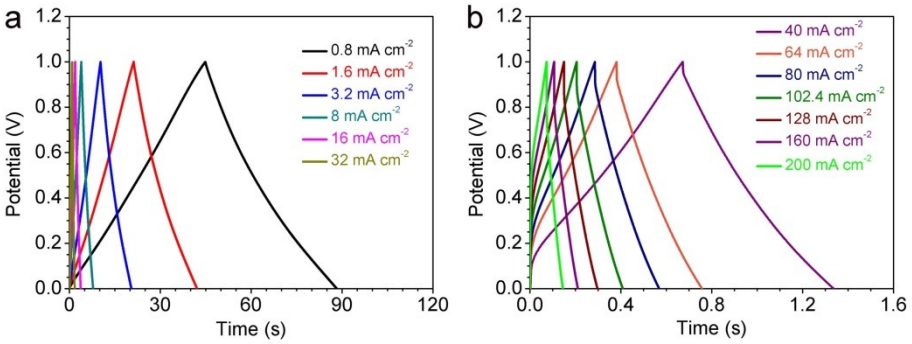

Fig. S10. Galvanostatic charge-discharge curves of rGO/CQDs-0.4 at different current densities ranging from 0.8 to 32 mA/cm^2 (a), and 40 to 200 mA/cm^2 (b) (No pressure applied). As the current density increases, the GCD curve of rGO/CQDs-0.4 maintains good symmetry.

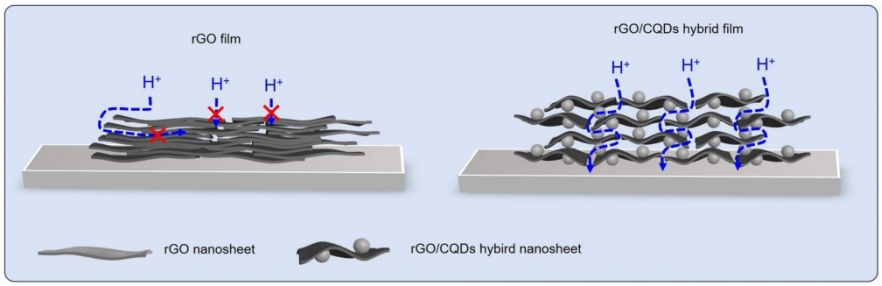

Fig. S11. Schematic illustration of ion migration within rGO film (left) and rGO/CQDs hybrid film (right).

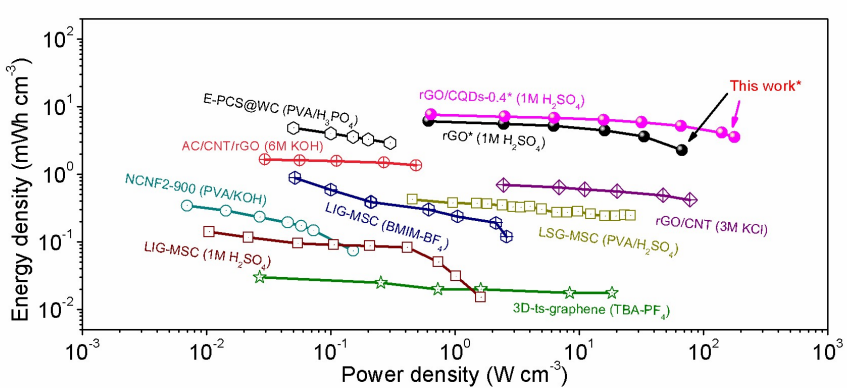

Fig. S12. Comparison of volumetric energy and power densities of the symmetric rGO/CQDs-0.4-based supercapacitor with rGO- and other carbon-based supercapacitors: laser-scribed graphene micro-supercapacitor (LSG-MSC),[4] laser-induced porous graphene micro-supercapacitor (LIG-MSC),[5] 3D turbostratic graphene (3D-ts-graphene),[6] porous carbon skeleton (E-PCS@WC),[7] active carbon/carbon nanotube/reduced graphene oxide composite filaments (AC/CNT/rGO),[8] reduced graphene oxide/carbon nanotube (rGO/CNT)[9] and NCNF2-900 (the N-self-doped carbon nanofiber is produced by carbonization of bacterial cellulose@zeolitic-imidazole frameworks hybrid aerogels at 900 °C for 2 h).[10]

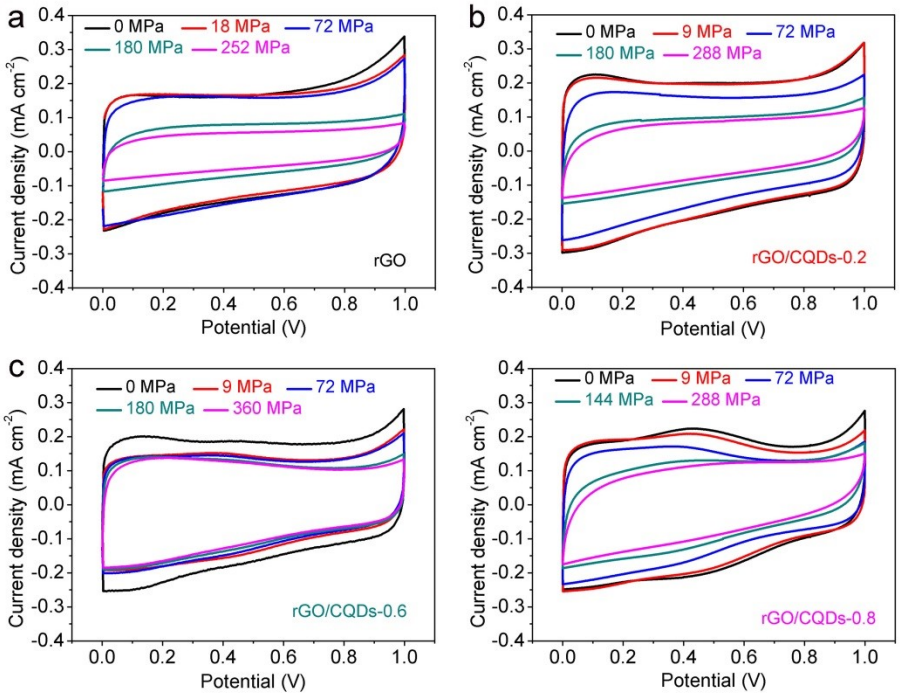

Fig. S13. Variations of the CV curves at 5 mV/s with increasing static pressure. (a) rGO, (b) rGO/CQDs-0.2, (c) rGO/CQDs-0.6 and (d) rGO/CQDs-0.8.

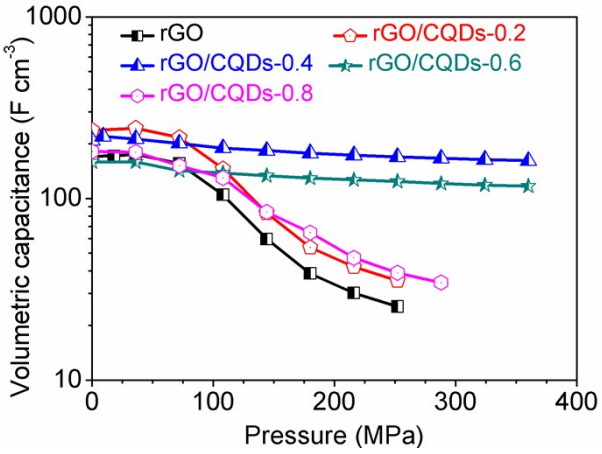

Fig. S14. Volumetric capacitances of the rGO and rGO/CQDs films loading with different CQD at 0.8 mA/cm^2 versus applied pressure.

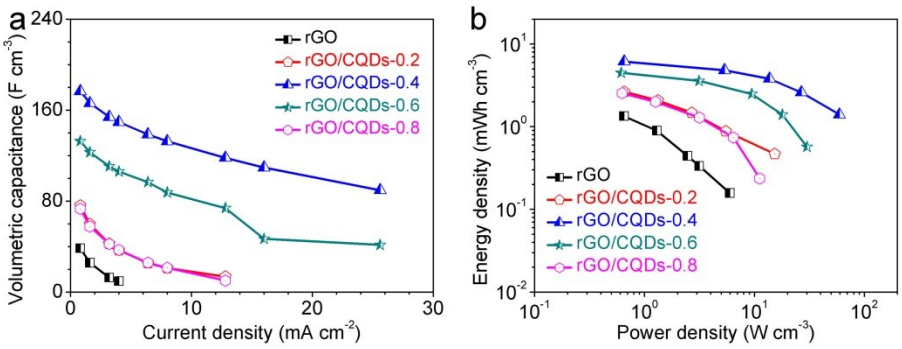

Fig. S15. Electrochemical performances of the rGO/CQDs and rGO films under a constant pressure of 180 MPa. (a) Volumetric capacitance at increasing current density. (b) Volumetric energy and power densities of rGO/CQDs- (with varying CQDs content: 0.2, 0.4, 0.6, and 0.8) and rGO-based supercapacitors.

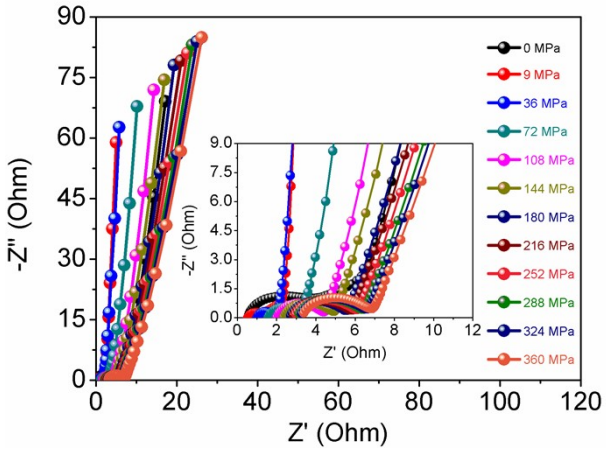

Fig. S16. Nyquist plots of rGO/CQDs-0.4-based supercapacitors under the static pressure ranging from 0 to 360 MPa.

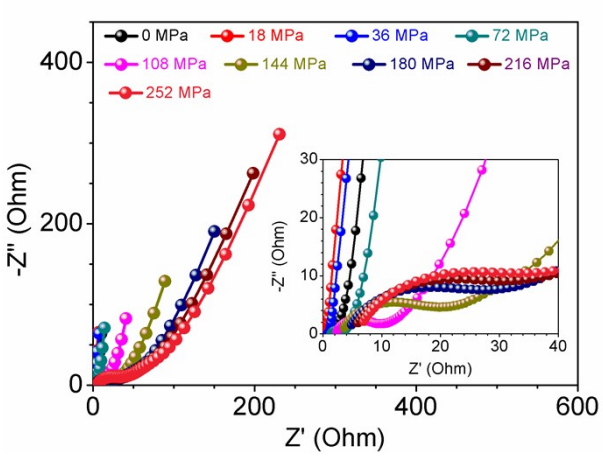

Fig. S17. Nyquist plots of rGO-based supercapacitor under the static pressure in the range from 0 to 252 MPa.

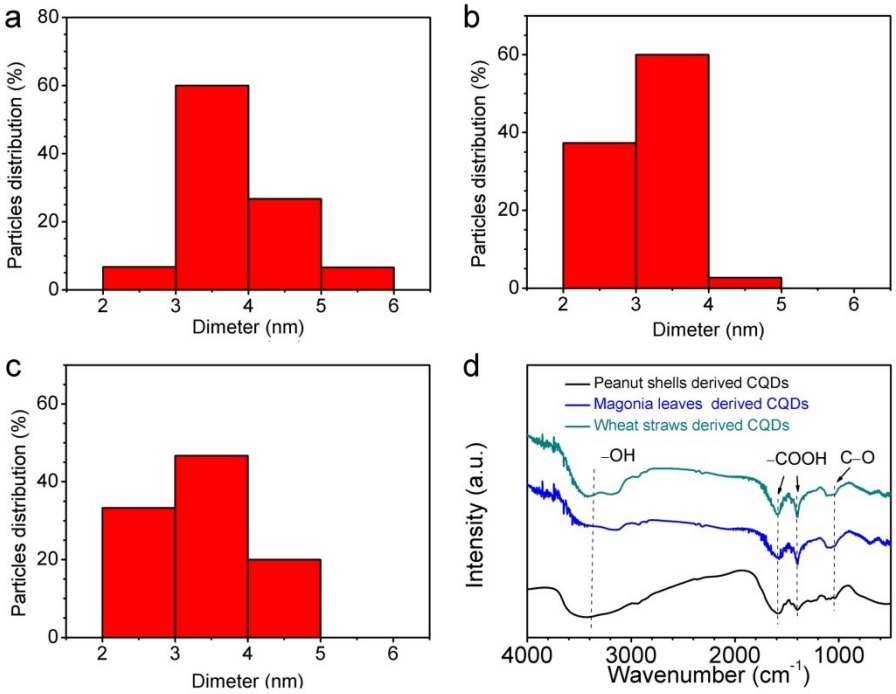

Fig. S18. Characterization of biological precursors-derived CQDs. The particle size distributions and Fourier Transform Infrared Spectroscopy (FTIR) spectra of CQDs synthesized from different biological precursors: peanut shells (a), magnolia leaves (b), and wheat straws (c).

The particle size distributions in Figs. S18a-c show that all CQDs primarily range between 2 and 6 nm in diameter. The FTIR spectrum in Figure S18d indicates that these CQDs share nearly identical surface functional groups, namely −COOH and −OH.

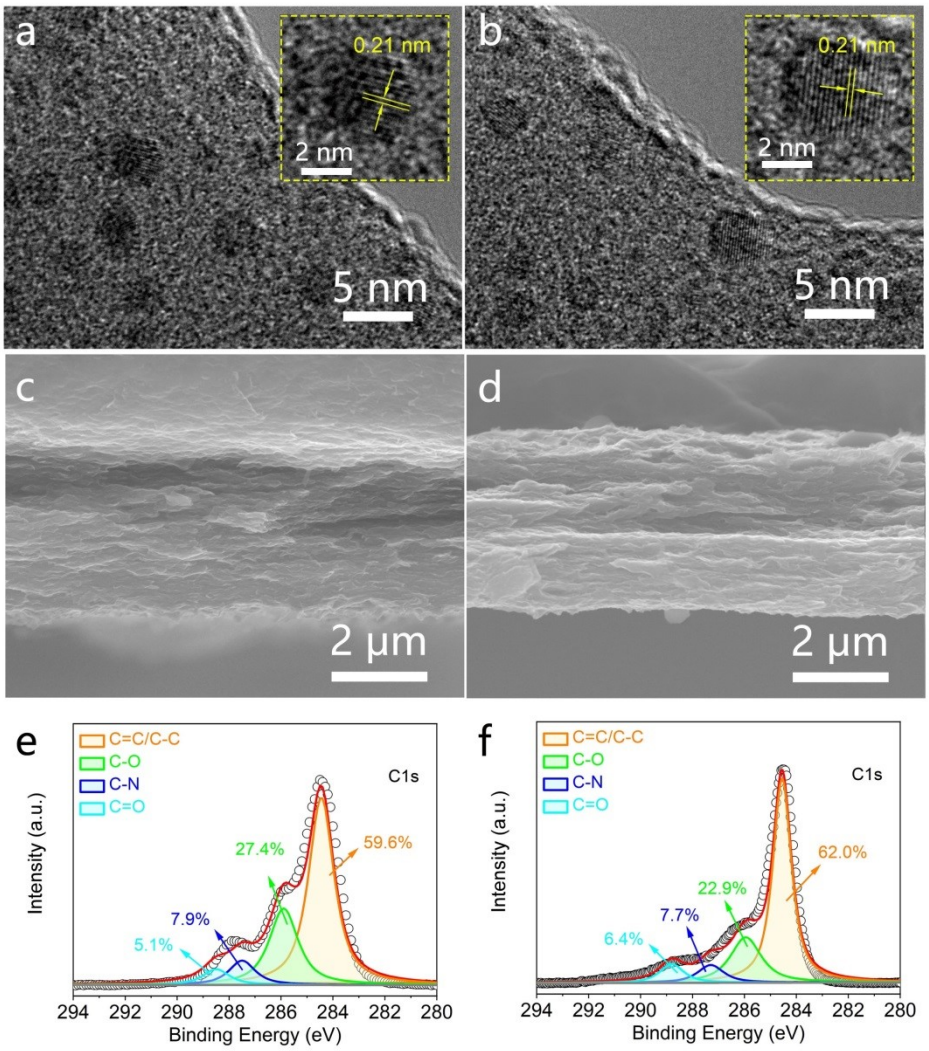

Fig. S19. Materials characterization of the rGO/CQDs-0.4 with CQDs synthesized with magnolia leaves and wheat straws as the precursors. (a-b) HRTEM image of rGO/CQDs hybrid nanosheets. (c-d) Cross-sectional SEM images of rGO/CQDs-0.4 hybrid films. (e-f) C1s XPS spectra. (a), (c) and (e) are the samples with magnolia leaves as the precursors. (b), (d) and (f) are the samples with wheat straws as the precursors.

Following the same preparation procedure for rGO/CQDs-0.4 (GO: CQDs mass ratio = 10:4), the resulting rGO/CQDs-0.4 samples synthesized using magnolia leaves and wheat straws as CQD precursors exhibit similar morphology and chemical composition compared to those prepared with peanut shells as the CQD precursor.

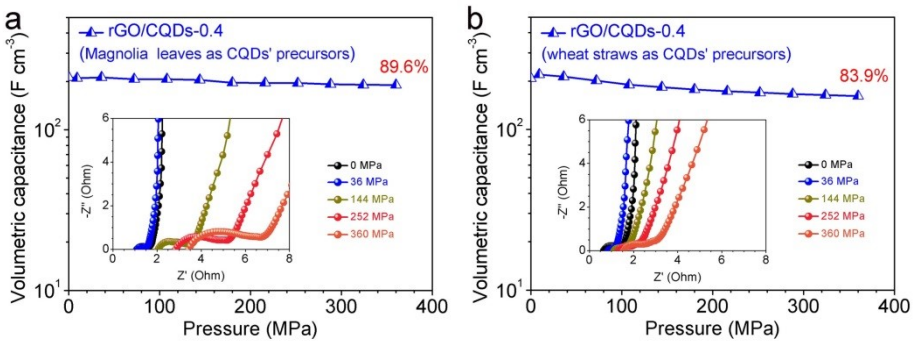

Fig. S20. Volumetric capacitances of the rGO/CQDs-0.4 electrodes with different CQDs' precursors at 0.8 mA/cm^2 and Nyquist plots (the insets) versus applied pressure. (a) Magnolia leaves as CQDs' precursors. (b) Wheat straws as CQDs' precursors.

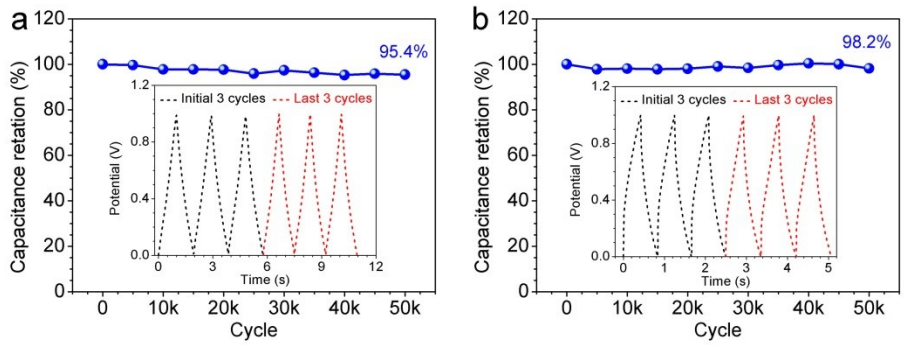

Fig. S21. Cycle performances of the rGO/CQDs-0.4-based supercapacitor at 32 mA/cm^2 under pressures of 36 MPa (a) and 180 MPa (b).

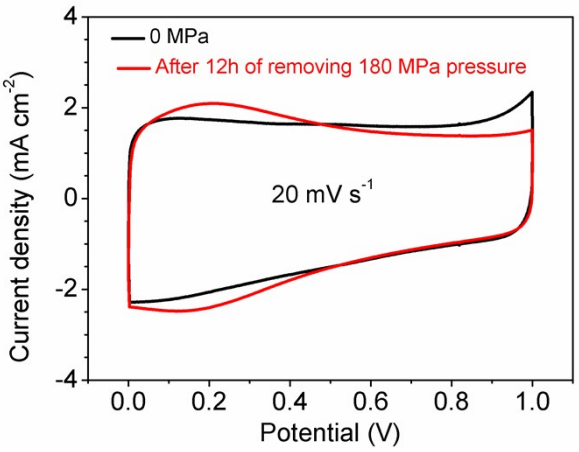

Fig. S22. CV curves of the rGO/CQDs-0.4-based supercapacitor at a scan rate of 20 mV/s: At 0 MPa pressure and after 180 MPa pressure removal for 12 h.

Even after the pressure is removed for 12 h, the CV curve displays minimal change in shape compared with its initial state. The enclosed area shows no significant decrease, indicating nearly complete capacitance recovery (almost 100%).

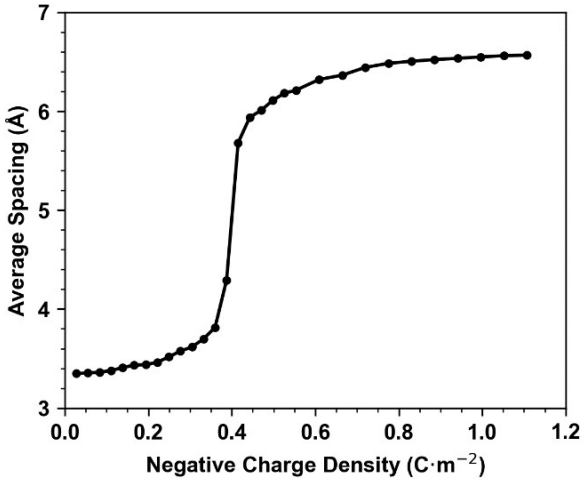

Fig. S23. Average interlayer spacing of rGO film plotted as a function of negative charge density per graphene sheet.

To simplify the simulation model, two assumptions were made: 1) the rGO sheets were considered flat and evenly separated in rGO film, and 2) both rGO and CQDs were assumed to be composed solely of carbon, excluding elements like hydrogen and oxygen.

Based on these assumptions, the average interlayer spacing *d* of rGO sheets in the rGO/CQDs films was calculated using[11, 12]

$$d = \frac{Areal\ mass\ density\ of\ rGO}{\rho_{rGO\ in\ rGO/CQDs\ film}}, \qquad (7)$$

and

$$\rho_{rGO\ in\ rGO/CQDs\ film} = \frac{m_{rGO/CDQs\ film} * f_g}{Volume\ of\ rGO/CQDs\ film}, \qquad (8)$$

where the areal mass density of rGO (graphene) is 0.77 mg/m^2,[11] $\rho_{rGO/CQDs\ film}$ is the packing density of rGO in rGO/CQDs film, $m_{rGO/CQDs\ film}$ is the mass of rGO/CQDs film, and f_g is the mass fraction of rGO in rGO/CQDs film. Following these calculations, the average interlayer spacings for rGO and rGO/CQDs-0.4 films were determined to be 0.54 and 0.76 nm, respectively.

Interlayer interactions in graphene films are governed by van der Waal forces[13], while Coulomb forces and proton transfer are described by ReaxFF.[14, 15] In previous reported molecular dynamics simulations, the electrode were regarded as immobile compared to ions, all carbon atoms in molecular dynamics model were kept rigid and fixed during the simulations[12, 16]. Here, when the pressures are applied on the electrodes, the carbon atoms are mobile due to the electrode deformation under high pressure. Take this into account, in the simulation, all carbon atoms in molecular dynamics model can't be kept fixed. However, rGO were assumed to be composed solely of carbon, excluding elements like hydrogen and oxygen,

thus the rGO can't maintain 0.54 nm average interlayer spacing due to van der Waals attractions of graphene sheet. To match the real case, i.e., a charge density of -0.42 C/m^2 per graphene sheet is chosen for the equilibrium of electrostatic repulsions and van der Waals attractions with an average interlayer spacing of 0.54 nm of rGO film. Accordingly, the -0.42 C/m^2 per graphene sheet is still chosen for rGO/CQDs film, and the CQDs are composed solely of carbon, and not charged.

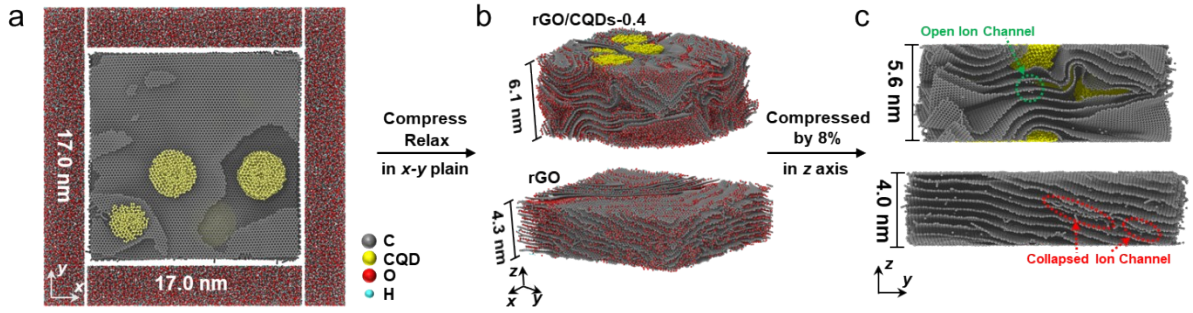

Fig. S24. Simulation of compression process. (a) Initial configuration: simulated rGO/CQDs-0.4 films surrounded by aqueous electrolyte. (b) Inherent structures: simulated rGO and rGO/CQDs-0.4 films, respectively, filled with aqueous electrolyte. (c) Deformation visualization: snapshot of simulated rGO and rGO/CQDs-0.4 films filled with aqueous electrolyte at a compressive strain of 8.0%. Only carbon atoms are shown to visualize the deformed structures of the films.

The entire simulation is divided into three steps:

Initial configuration: rGO and rGO/CQDs-0.4 (exemplified in Fig. S24a) are surrounded by a 2 M H^+ aqueous electrolyte containing hydronium ions and water molecules. The total number of atoms simulated is 178,653 for rGO and 209,458 for rGO/CQDs-0.4 with the electrolyte. Periodic boundary conditions (PBCs) are applied in the z dimensions, while non-periodic and shrink-wrapped boundary conditions are used in the x and y dimensions.

Compression and equilibration: rGO and rGO/CQDs-0.4 films are gradually filled with the aqueous electrolyte in a micro-canonical ensemble using cyclic compression (strain rate of 10^9 s^{-1}) in the x and y dimensions, coupled with a Langevin thermostat set to 300 K. The resulting equilibrated structures of both films filled with electrolyte are obtained using the conjugate-gradient method (Fig. S24).

Final compression: The electrolyte-filled rGO and rGO/CQDs-0.4 films are further compressed in the z-dimension at a strain rate of 10^9 s^{-1}. Snapshots of the simulations at a strain of 8.0% are shown in Fig. S24c, where only carbon atoms are retained to visualize the deformation of the graphene layers after compression.

Table S1. Calculated pressure applied facility on rGO/CQDs hybrid-films based supercapacitors.

Displayed pressure of manual powder tablet press (MPa)	Calculated pressure (MPa)
0	0
0.1	9
0.2	18
0.4	36
0.8	72
1.2	108
1.6	144
2	180
2.4	216
2.8	252
3.2	288
3.6	324
4	360

Table S2. Comparison of the energy and power performance of rGO/CQDs-based supercapacitors with carbon-based supercapacitors in reported literatures.

Material	Electrolyte	Density (g/cm^3)	Mass loading of single electrode (mg/cm^2)	E_{vol} @P_{vol} (mWh/cm^3@W/cm^3)	$P_{vol\ max}$ (W/cm^3)	Ref.
HPGM	6 M KOH	1.58	/	13.1@0.0395	5.9	[17]
YP80/G	6 M KOH	0.76	/	4.04@0.038	2.04	[18]
rGO/SWCNT-1	PVA/H_2SO_4	1.59	/	9.98@~0.023	~0.35	[19]
VArGO	6 M KOH	1.18	12.3	7.3@0.21	2.05	[20]
F-GRF	6 M KOH	0.92	21	11.5@0.0827	~2.5	[21]
CoDC-0.5	6 M KOH	0.97	25	9.1@0.0679	1.21	[22]
E-PCS@WC	1 M Na_2SO_4	/	/	4.86@0.022	~1.15	[7]
SLC	6 M KOH	~0.45	14.4	2.6@0.0285	2.255	[23]
rGO/CQDs-0.4	**1 M H_2SO_4**	**1.38**	**0.45**	**7.63@0.064**	**177.1**	**This work**
rGO/CQDs-0.4	**1 M H_2SO_4**	**1.38**	**0.63**	**7.28@0.11**	**249.1**	
rGO/CQDs-0.4	**1 M H_2SO_4**	**1.36**	**11.7**	**6.88@0.094**	**7.8**	
rGO/CQDs-0.4	**6 M KOH**	**1.38**	**0.63**	**7.25@0.46**	**170.1**	
rGO/CQDs-0.4	**6 M KOH**	**1.36**	**11.7**	**6.21@0.121**	**7.0**	

The involved abbreviations are:

HPGM: high density porous graphene macroform

YP80/G: commercial AC YP80/graphene

rGO/SWCNT-1: reduced graphene oxide/carbon nanotube single-walled carbon nanotube-1;

VArGO: vertically aligned reduced graphene oxide;

CoDC-0.5: ultramicroporous carbons-0.5;

F-GRF: multilayer-folded graphene ribbon films;

E-PCS@WC: porous carbon skeleton.

References

[1] Pech, D., Brunet, M., Durou, H., Huang, P., Mochalin, V., Gogotsi, Y., Taberna, P.-L., and Simon, P. Nat. Nanotechnol. 5 (2010) 651-654.
[2] Taberna, P. L., Simon, P., and Fauvarque, J. F. J. Electrochem. Soc. 150 (2003) A292.
[3] Di Fabio, A., Giorgi, A., Mastragostino, M., and Soavi, F. J. Electrochem. Soc. 148 (2001) A845.
[4] El-Kady, M. F., and Kaner, R. B. Nat. Commun. 4 (2013) 1475.
[5] Lin, J., Peng, Z., Liu, Y., Ruiz-Zepeda, F., Ye, R., Samuel, E. L. G., Yacaman, M. J., Yakobson, B. I., and Tour, J. M. Nat. Commun. 5 (2014) 5714.
[6] Strauss, V., Marsh, K., Kowal, M. D., El-Kady, M., and Kaner, R. B. Adv. Mater. 30 (2018) 1704449.
[7] Ouyang, J., Wang, X., Wang, L., Xiong, W., Li, M., Hua, Z., Zhao, L., Zhou, C., Liu, X., Chen, H., and Luo, Y. Carbon 196 (2022) 532-539.
[8] Gao, T., Zhou, Z., Yu, J., Zhao, J., Wang, G., Cao, D., Ding, B., and Li, Y. Adv. Energy Mater. 9 (2019) 1802578.
[9] Beidaghi, M., and Wang, C. Adv. Funct. Mater. 22 (2012) 4501-4510.
[10] Chen, H., Liu, T., Mou, J., Zhang, W., Jiang, Z., Liu, J., Huang, J., and Liu, M. Nano Energy 63 (2019) 103836.
[11] Yang, X., Cheng, C., Wang, Y., Qiu, L., and Li, D. Science 341 (2013) 534.
[12] Bo, Z., Yang, J., Qi, H., Yan, J., Cen, K., and Han, Z. Energy Storage Mater. 31 (2020) 64-71.
[13] Kozioł, Z., Gawlik, G., and Jagielski, J. Chin. Phys. B 28 (2019) 096101.
[14] Kański, M., Hrabar, S., van Duin, A. C. T., and Postawa, Z. J. Phys. Chem. Lett. 13 (2022) 628-633.
[15] Zhang, W., and van Duin, A. C. T. J. Phys. Chem. B 121 (2017) 6021-6032.
[16] Yang, H., Yang, J., Bo, Z., Chen, X., Shuai, X., Kong, J., Yan, J., and Cen, K. The J. Phys. Chem. Lett. 8 (2017) 3703-3710.
[17] Tao, Y., Xie, X., Lv, W., Tang, D.-M., Kong, D., Huang, Z., Nishihara, H., Ishii, T., Li, B., Golberg, D., Kang, F., Kyotani, T., and Yang, Q.-H. Sci. Rep. 3 (2013) 2975.
[18] Li, P., Li, H., Han, D., Shang, T., Deng, Y., Tao, Y., Lv, W., and Yang, Q.-H. Adv. Sci. 6 (2019) 1802355.
[19] Zhong, J., Sun, W., Wei, Q., Qian, X., Cheng, H.-M., and Ren, W. Nat. Commun. 9 (2018) 3484.
[20] Yoon, Y., Lee, K., Kwon, S., Seo, S., Yoo, H., Kim, S., Shin, Y., Park, Y., Kim, D., Choi, J.-Y., and Lee, H. ACS Nano 8 (2014) 4580-4590.
[21] Sheng, L., Chang, J., Jiang, L., Jiang, Z., Liu, Z., Wei, T., and Fan, Z. Adv. Funct. Mater. 28 (2018) 1800597.
[22] Zhang, S., Zhu, J., Qing, Y., Wang, L., Zhao, J., Li, J., Tian, W., Jia, D., and Fan, Z. Adv. Funct. Mater. 28 (2018) 1805898.
[23] Li, H., Yuan, D., Tang, C., Wang, S., Sun, J., Li, Z., Tang, T., Wang, F., Gong, H., and He, C. Carbon 100 (2016) 151-157.